Discover Nano

Research

Efficient photocatalytic methylene blue dye degradation from green-synthesized silver-doped iron oxide ($Ag@Fe_2O_3$) nanostructures

Vikram Jadhav[1] · Yash Dhanwate[1] · Pradnya Raut[2] · Shilpa Shinde[2] · Rajashri Sawant[3] · Arun Bhagare[1]

Received: 17 December 2024 / Accepted: 17 March 2025
Published online: 04 April 2025

Abstract

This study presents an environmentally friendly method for synthesizing $Ag@Fe_2O_3$ nanostructures through a hydrothermal technique that utilizes *Saussurea obvallata* leaf extract as a reducing and capping agent. The material was characterized using UV–Vis, FTIR, XRD, SEM–EDX, and TEM-SAED-line profile analysis. The UV–Vis shows a maximum absorbance peak at 380 nm, showing a band gap of 3.26 eV. FTIR analysis revealed several functional groups (vibrational modes), including 944 and 514 cm^{-1} (Fe–O) and 445 cm^{-1} (Ag–O). XRD spectra analysis confirmed the crystalline nature and, using the Scherrer equation, showed an average crystallite size of 49.57 nm. EDX confirmed the presence of only Ag, Fe, and O elements. SEM and TEM-SAED analyses revealed an *echinus*-like morphology with an interplanar spacing of 126 pm of the nanostructures. The photocatalytic activity of $Ag@Fe_2O_3$ was investigated through the degradation of methylene blue (MB) dye in the presence of UV–visible light irradiation. It was observed that 97.10% MB dye degradation occurred within 60 min, with the rate constant and half-life being 0.03025 min^{-1} and 22.90 min, respectively. It was deduced that the synergistic interaction of Ag with Fe_2O_3 promoted the separation of charge, significantly diminishing electron–hole recombination. This research presents plant extract as a readily available, cost-effective, and environmentally friendly way to produce highly efficient photocatalysts for degrading wastewater dye compounds.

Article Highlights

- The synthesized $Ag@Fe_2O_3$ nanostructure using*Saussurea obvallata* leaf extract for a biogenic synthesis method shows excellent photocatalytic dye degradation of methylene blue under UV-visible light irradiation.
- The combination of Ag & Fe_2O_3nanoparticles improved the charge separation efficiency & reduced electron-hole pair recombination, leading to enhanced photocatalytic performance.
- The nanostructure achieved a high photocatalytic dye degradation rate of 97.10 % within 60 minutes, with a reaction rate constant & half-life of 0.03025 min^{-1} & 22.90 min, resp. The biogenic synthesis method is a sustainable & cost-effective approach to producing efficient photocatalysts for several environmental remediations.

Keywords $Ag@Fe_2O_3$ · Biogenic synthesis · *Saussurea obvallata* plant · Dye degradation · Methylene blue

✉ Vikram Jadhav, mevikramjadhav@gmail.com; ✉ Pradnya Raut, pradnyar_ioe@bkc.met.edu; ✉ Rajashri Sawant, rajashriahire@gmail.com | [1]Department of Chemistry, M.V.P. Samaj'S K. K. Wagh Arts, Science, and Commerce College, Pimpalgaon (B.), Nashik, Maharashtra 422209, India. [2]MET's Institute of Engineering, Bhujbal Knowledge City, Adgaon, Nashik, Maharashtra 422207, India. [3]M.P.H. Arts, Science, and Commerce Mahila College, Malegaon, Maharashtra 423105, India.

1 Introduction

Recent research has observed that environmental pollutant degradation is a critical global issue. Among the countless amounts of pollutants, organic dyes, such as methylene blue (MB), have been reported due to their high toxicity and carcinogenic nature, leading to a significant threat to human health and aquatic environments [1–4]. Developing effective and sustainable methods for organic dye degradation is considered a vital issue. Traditional removal methods include adsorption and chemical oxidation; generally, these methods suffer from decreased efficiency and secondary pollution, as well as expensive [5, 6]. As for these disadvantages or limitations, photocatalysis is a promising process in environmental remediation due to its efficient activity, cost-effectiveness, and environmental friendliness. Some other examples of photocatalysts are metal oxide semiconductors such as ZnO, TiO_2, CaO, and MgO. They can absorb photonic energy and generate electron–hole (e^- & h^+) pairs. These pairs interact with H_2O or O_2 molecules to produce very reactive species/radicals such as $^{\bullet}OH$ and $^{\bullet}O_2^-$, capable of oxidizing the organic pollutants into harmless products. However, rapid regeneration of photogenerated charge carriers, insufficient light absorption, and a lack of active sites have often degraded the efficiency of photocatalytic processes. Overcoming these challenges has been addressed through nanocomposite material synthesis, modification of photocatalyst surface properties, and UV–visible light-sensitive photocatalysts [7–10].

Recently, due to their unique physicochemical characteristics/properties and broad applicability, the Ag@Fe_2O_3 nanostructure has gained considerable importance in the research field. Hybrid nanomaterials combined with Ag and Fe_2O_3 nanoparticles the unique properties have drawn significant interest because of their potential applicability in catalysis, biomedical applications, and environmental remediation. Such an enhanced photocatalytic property of Ag has shown itself by being an effective antibacterial and antifungal agent that can aid Fe_2O_3 material to improve its potential based on photocatalytic activity as an electron acceptor, thus reducing recombination of charge carriers with elevated radical generation [11–14]. Multiple syntheses for Ag@Fe_2O_3 nanostructures have also been investigated via methods such as chemical reduction, sol–gel, and green syntheses [15–18]. Here, plant extracts perform the role of reductants and capping agents during nanostructure synthesis, providing well-dispersed and stabilized nano-size particles [19, 20]. Different plant extract sources report the successful synthesis of Ag@Fe_2O_3 nanostructures, including *Azadirachta indica, Citrus sinensis, Aloe vera*, etc. These nanomaterials, synthesized through green methodologies, show potential photocatalytic dye degradation activity [18, 21–24].

Saussurea obvallata, or the snow lotus (Fig. 1), is a rare medicinal flora growing at high altitudes in the Himalayas. Tibetan and Chinese traditional medicines have been used for centuries to treat various health conditions, ranging from respiratory disorders to inflammation and pain management. The plant's bioactive contents, such as flavonoids, phenolic acids, and essential oils, can uniquely differentiate it for medicinal effectiveness [25–27]

In the past ten years, *Saussurea obvallata* has attracted much attention and concern from scholars due to its potential for the medicine, cosmetics, and food industries. Its antioxidant, anti-inflammatory, and antimicrobial activity was tested and published in several scientific papers. However, the extensive harvesting within the species' natural habitat led to its decline in population. Thus, there is a need for sustainable planting and conservation strategies. The plant contains several bioactive compounds like flavonoids and phenolic acids that are good natural reducing and capping agents for synthesizing nanomaterials. In this role, plant extracts are advantageous due to being cost-effective, available, non-toxic, and environmentally sustainable [26–28].

Fig. 1 *Saussurea obvallata* plant leaf

The research comes with valuable novelty in suitable photocatalysis methods for environment remediation. This is one essential integration of the green synthesis approaches used to synthesized nanostructures to improve catalytic behavior. It ensures that environmentally friendly strategies are undertaken to reduce the use of hazardous chemicals in nature. Photocatalytic degradation using such nanostructures towards visible-light-driven MB dye was investigated throughout the work. It is an example of a pollutant commonly identified and dealt with across environmental contamination aspects. This innovative approach uses visible light to make the degradation process more energy-efficient and effective than traditional UV light methods. We emphasize how applying doped Ag@Fe_2O_3 would improve the photocatalysis activity, potentially raising the degradation rate and increasing efficiency when removing pollutants in water sources. Kinetic studies were conducted to evaluate the rates of the photocatalytic reactions. Kinetics is essential for optimizing the performance of catalysts and ensuring their practical applicability in real-world scenarios. We can show how the findings from these studies contribute to the general understanding of catalyst efficiency and reusability, which are essential for sustainable practices in environmental remediation. Besides that, this introduction can also be supported by a discussion of the ecological aspects of applying these nanostructures to dye degradation. These nanostructures have significant advantages as materials since they facilitate the removal of organic dyes and other harmful pollutants. Hence, there is significance in cleaning up environmental issues. This should be understood against the backdrop of how the physical characteristics of nanoparticles affect their catalytic performance. Thus, the novelty of this study is a combined effect, namely green synthesis, visible light activation, and effective MB dye degradation using nanostructures. Therefore, in the present study, we have reported the synthesis of eco-friendly Ag@Fe_2O_3 nanostructures using *Saussurea obvallata* plant extract and their characterization using several analytical methods. The synthesized nanostructures exhibited photocatalytic MB dye degradation activity in UV–Vis irradiation; the 97.10% degradation rate was observed within 60 min. This efficient photocatalytic dye degradation may be the synergistic interactions of Ag and Fe_2O_3 nanoparticle material, facilitating effective charge separation and hindering electron–hole regeneration. This work offers a new, environmentally friendly route to highly efficient photocatalysts with potential environmental remediation applications.

2 Materials and methods

2.1 Materials

Precursors: Iron (III) chloride hexahydrate ($FeCl_3{\cdot}6H_2O$) (AR-grade, purity ≥ 99%) & Silver nitrate ($AgNO_3$) (AR-grade, purity ≥ 99.8%). Chemicals: Ethanol (C_2H_5OH) (AR-grade, purity ≥ 99.8%). Sodium hydroxide (NaOH) (AR grade, purity ≥ 98%) and Deionized water (Chargo chemicals). Plant material: Saussurea obvallata was domestically cultivated, and its fresh leaves were collected from a local agricultural farm, Pimpalgaon (B) 422209, Nashik, Maharashtra.

2.2 Methods

2.2.1 Preparation of *Saussurea obvallata* leaf extract

The healthy and fresh *Saussurea obvallata* leaves were collected and cleaned using deionized water to remove any unwanted contaminates. The leaves were dried in the oven at 60 °C and then powdered using a mortar and pestle. 1 g of powdered leaves was introduced into 100 mL de-ionized water and then reflux extracted for a specific period. The extract from this process was then filtered to remove any solid particulate matter.

2.2.2 Synthesis of Ag@Fe_2O_3 nanostructure using plant leaves extract

A green synthesis protocol based on the convenient pathway was used to synthesize Ag@Fe_2O_3 nanostructures by extracting *Saussurea obvallata* leaves. 0.05 M $FeCl_3{\cdot}6H_2O$ (7.5 mL), 0.02 M $AgNO_3$ (7.5 mL), and 15 mL leaf extract were mixed in a beaker, stirred for 30 min, maintained pH around 10 using sodium hydroxide solution, and the solution was sonicated to ensure proper mixing of the reactants. The Teflon autoclave was used, and the hydrothermal method (120 °C; 7 h) was applied to the solution. After cooling, the solution was filtered, and the precipitated product was washed using deionized water and ethanol to eliminate the remaining impurities. The obtained precipitate dried at 60 °C (6 h) using an oven, followed by calcination at 300 °C for 3 h to produce the Ag@Fe_2O_3 nanostructures (Fig. 2), and it was used for further characterization.

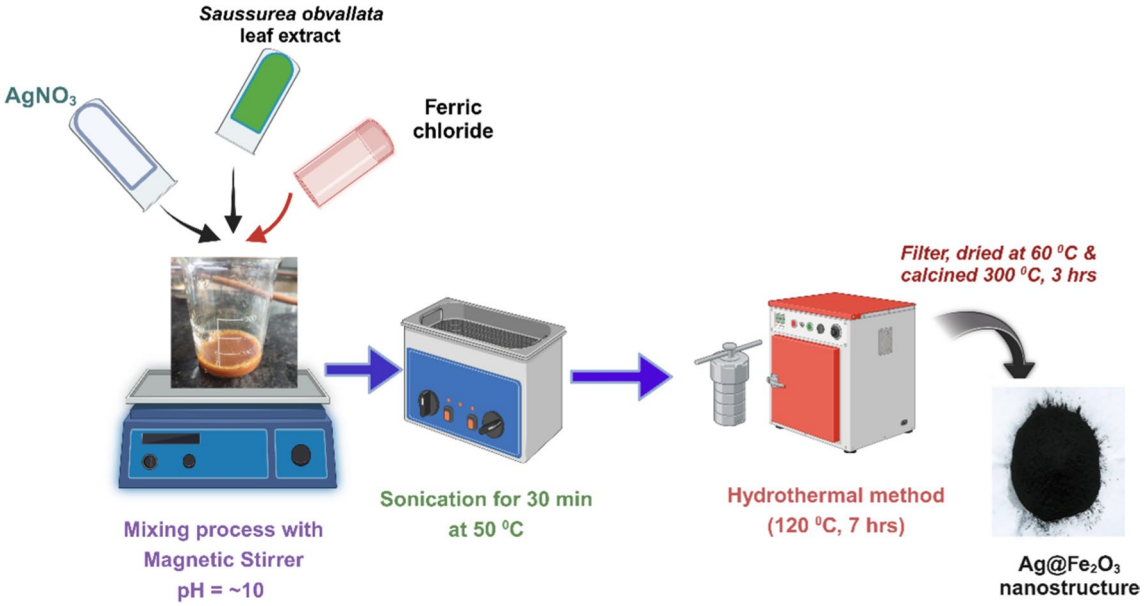

Fig. 2 Experimental method of synthesis of $Ag@Fe_2O_3$ nanostructure

2.2.3 Photocatalytic MB dye degradation method

The experimental protocol was set up to study the photocatalytic degradation of MB dye using $Ag@Fe_2O_3$ nanostructures. First, the reaction mixture was prepared by dissolving a 10^{-5} M MB dye and adding 10 mg of $Ag@Fe_2O_3$ to 100 mL of the dye solution. A preliminary dark adsorption experiment was carried out to assess the contribution of adsorption. The reaction mixture was kept in a dark environment for 10 min to enable the adsorption of the dye onto the catalyst surface without any photocatalytic activity. The reaction mixture was then exposed to a UV–Vis source for 60 min. Reaction mixture samples were drawn at appropriate intervals to measure the absorbance using a spectrophotometer. The UV/Vis spectrum of the samples was calculated to find differences in absorption at 662 nm, which is the characteristic maximum of absorption for MB. The absorbance maxima of the dye was found to decrease due to the decrease observed at 662 nm. The synergistic interactions between the Ag and Fe_2O_3 material of the $Ag@Fe_2O_3$ nanostructures were responsible for the enhanced activity. The Ag trapped electrons, thus inhibiting charge carrier regeneration and promoting the formation of radicals, which are very potent oxidizing agents for organic pollutants [12, 29].

To calculate the percentage of MB dye degradation, the following formula (Eq. 1) was used;

$$\%\ of\ MB\ dye\ degradation = \frac{[A]_0 - [A]}{[A]_0} x100 \tag{1}$$

where $[A]_0$ = Initial absorbance (t = 0 min) and [A] = Absorbance (t = t min).

3 Results and discussion

3.1 UV–Vis analysis

The spectra of the $Ag@Fe_2O_3$ nanostructure are given in Fig. 3, showing strong bands at ~ 380 nm may be interpreted for surface plasmon resonance (SPR) phenomena [22].

A red-shift in the SPR band compared to the pure Ag nanoparticles, generally at ~ 400 nm, indicates successful synthesis of the $Ag@Fe_2O_3$ nanostructures. The band gap (E_g) value was calculated using the following formula (Eq. 2) (λmax = 380 nm) [16]:

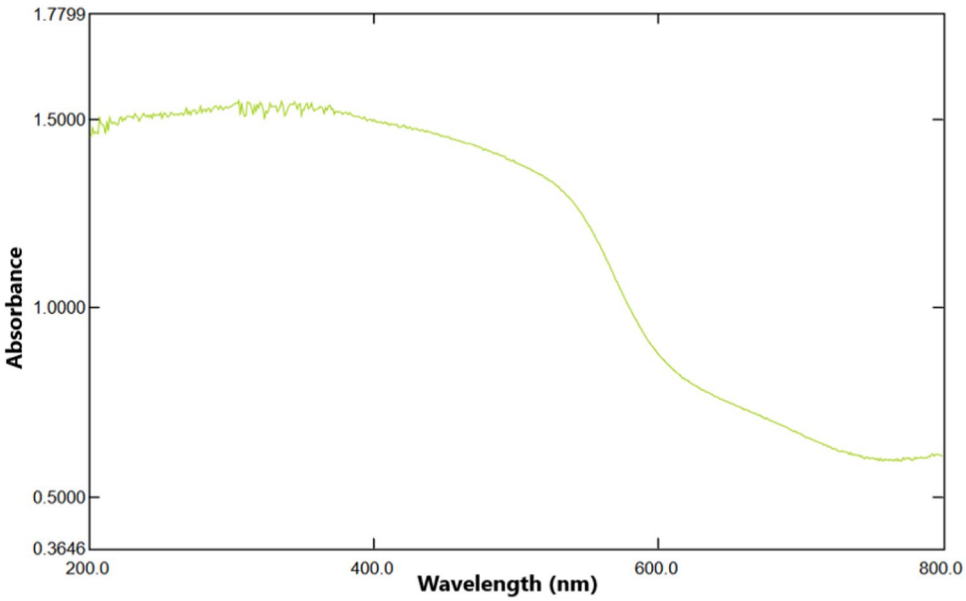

Fig. 3 UV–Vis spectra of Ag@Fe_2O_3 nanostructure

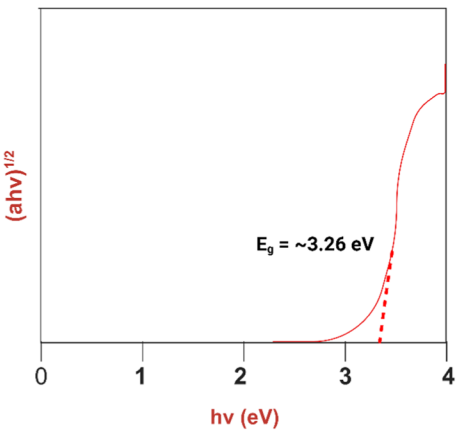

Fig. 4 Tauc plot of Ag@Fe_2O_3 nanostructure

$$Eg = \frac{1240}{\lambda \max} \tag{2}$$

$$= \frac{1240}{380}$$

$$= 3.26eV \tag{3}$$

The Tauc plot is a graphical presentation used in determining the bandgap of material from their optical absorption spectra (Fig. 4). For the nanostructure, the direct bandgap was found in the plot, which ranges to 3.26 eV (Eq. 3). Band gap is one of the important factors that control the photocatalytic efficiency as the generation of the electron–hole pair is also affected due to the absorption of visible light. For instance, the band gap of Fe_2O_3 can be engineered through doping; various studies revealed that doping carbon or silver materials alters the band gap and thus increases the photocatalytic activity. The Ag@Fe_2O_3 showed a direct band gap at 3.26 eV, meaning it will be able to absorb visible light. This means that the material may very well absorb UV light, consistent with the absorption spectrum, where a sharp absorption peak in the ultraviolet region is observed. This is because a relatively high band gap energy would involve the highly energetic generation of electron–hole charge carrier pairs when subjected to photoexcitation; this, in paradoxical interaction, degrades the organic pollutants through catalysis [30, 31].

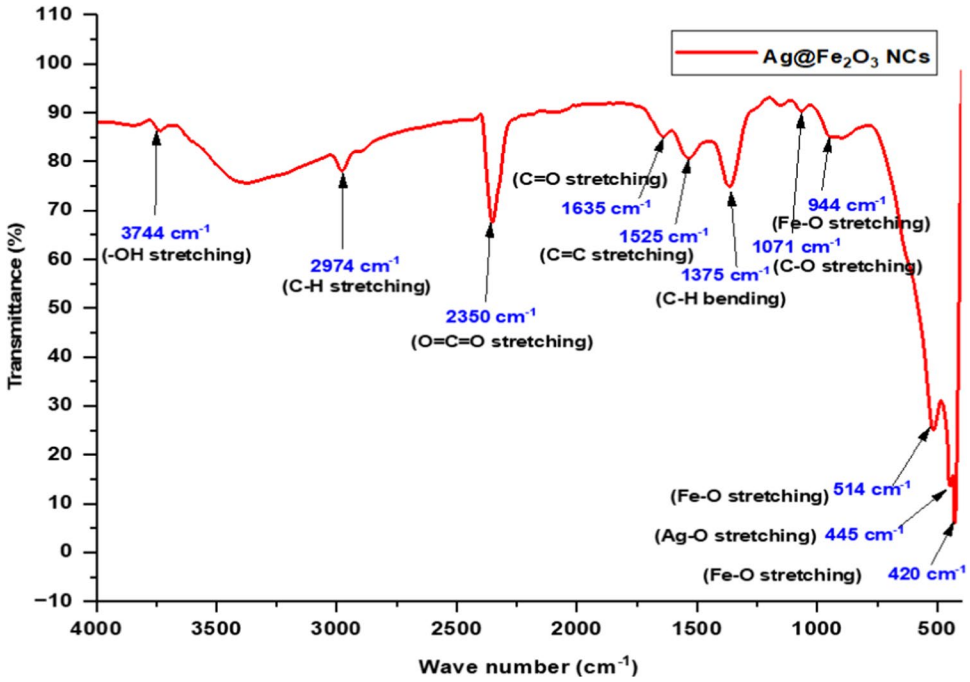

Fig. 5 FTIR spectra of Ag@Fe_2O_3 nanostructure

3.2 FTIR analysis

Ag@Fe_2O_3 nanostructure reveals distinct characteristic peaks in FTIR spectra at 3744, 2974, 2350, 1635, 1525, 1375, 1071, 944, 514, 445, and 420 cm^{-1} as shown in Fig. 5.

These peaks are indicative of the following functional groups, 3744 cm^{-1}: O–H group, 2974 cm^{-1}: C–H stretching (aliphatic), 2350 cm^{-1}: O=C=O stretching modes, 1635 cm^{-1}: C=O stretching groups, 1525 cm^{-1}: C=C stretching (aromatic) groups, 1375 cm^{-1}: C–H bending (methyl) groups, 1071 cm^{-1}: C–O stretching (alcohols or ethers), 944, 524 & 420 cm^{-1}: Fe–O stretching (Fe_2O_3), 445 cm^{-1}: Ag–O stretching (silver oxide). Detecting these functional groups substantiates the successful synthesis of the Ag@Fe_2O_3 nanostructure. 3744 & 2974 cm^{-1} may exist the O–H & C–H groups (originate from plant leaves) on the nanostructure's surface, contributing to its photocatalytic properties. The C=O and C=C stretching peaks noted at 1635 and 1525 cm^{-1} may result from the existence of oxidized organic compounds. The Fe–O stretching peaks at 944, 514, and 420 cm^{-1} affirm the presence of Fe_2O_3 within the nanomaterial matrix. The Ag–O stretching peak at 445 cm^{-1} corroborates the presence of silver oxide in the nanomaterial [30–34].

3.3 XRD analysis

The XRD pattern of the as-prepared Ag@Fe_2O_3 is shown in Fig. 6.

The strong peaks positioning at 33.25°, 35.74°, 49.83°, 54.99°, and 64.190 correspond to the (104), (110), (024), (116), and (300) lattice planes of the BCC phase of Fe_2O_3 resp. (JCPDS card No. 00–024-0072) [35], there are five additional peaks at 2θ = 27.92°, 32.26°, 46.33°, 57.49°, and 76.82° correspond to the (210), (113), (124), (240), and (300) lattice planes of the FCC lattice of Ag in Ag@Fe_2O_3 [36]. These peaks confirmed the Ag and Fe_2O_3 in the Ag@Fe_2O_3 nanostructure. The mean crystallite size of the Ag@Fe_2O_3 is 49.57 nm, which is calculated using the Scherrer equation [10]. The Rietveld refinement method analyzes the XRD pattern and is applied to refine a structural model for extracting precise lattice parameters, phase fractions, etc. The method fits the entire diffraction pattern into the theoretical model, through which one determines various structural parameters such as the lattice constants, atomic positions, thermal factors, etc. [37].The XRD patterns of the obtained data indicate that the clear peaks of Ag and Fe_2O_3 with no shifting are due to Schottky junctions between Ag and Fe_2O_3. Therefore, analysis in this way is important because it helps establish the structural property of the nanostructure Ag@Fe_2O_3, which may relate to function properties and antibacterial activity [37, 38].

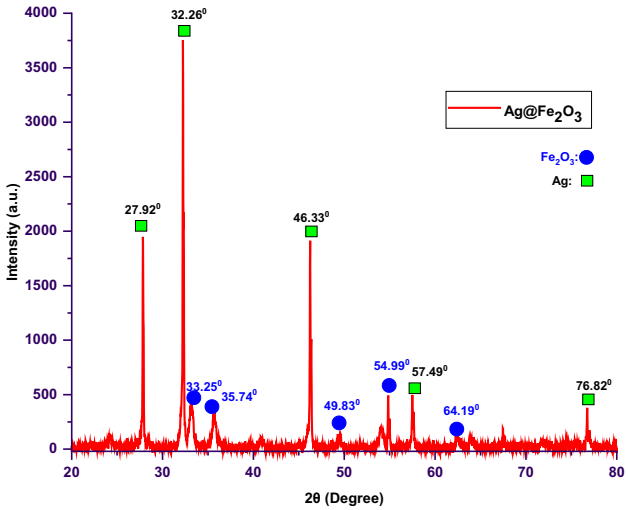

Fig. 6 XRD spectra of Ag@Fe_2O_3 nanostructure

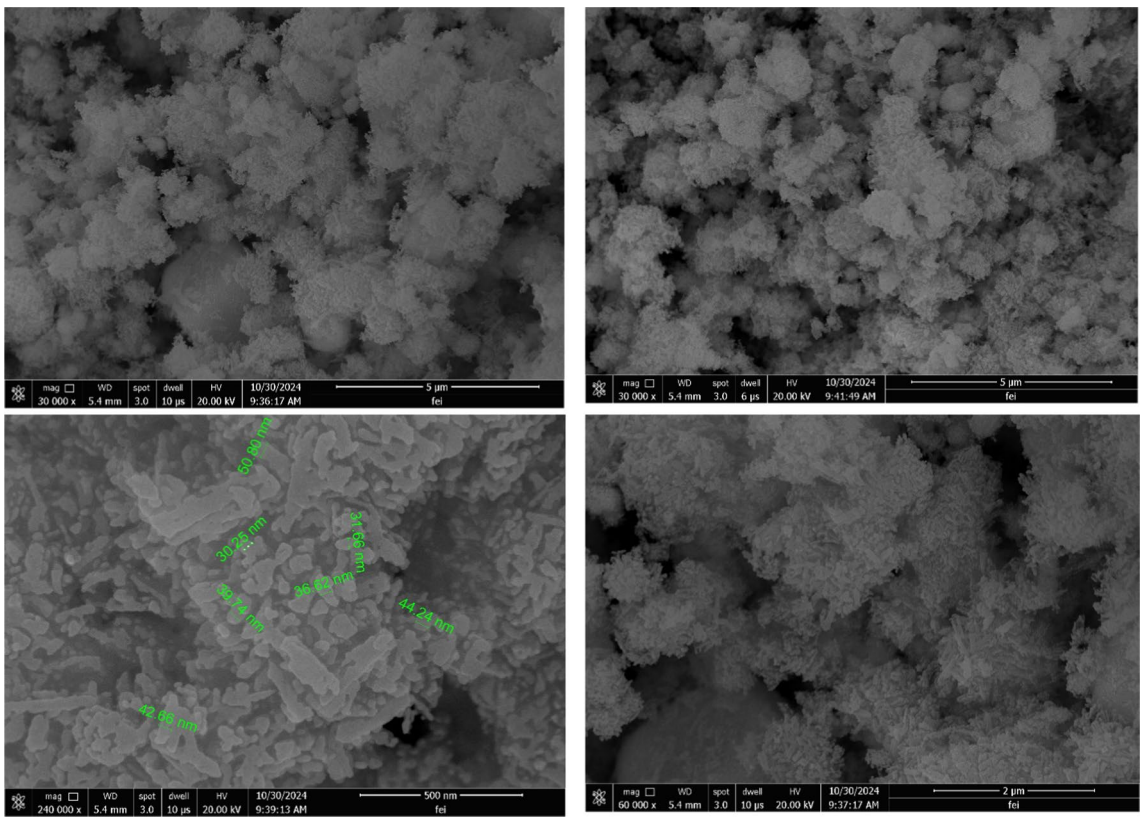

Fig. 7 SEM images of Ag@Fe_2O_3 nanostructure

3.4 SEM–EDX analysis

The morphology of the synthesized nanostructures was analyzed using SEM analysis (Fig. 7). These images show an *echinus*-like morphology (average particle size ~ 35 nm) with a relatively homogenous distribution of particles.

Irregularly shaped and porous particles greatly enhance their surface area, thus permitting the absorption of organic dye impurities more intensively and producing higher contact areas for the interaction of catalysts and MB dye molecules. This effect is more observable in the Fe_2O_3-based photocatalysts, which add Ag to enhance photocatalytic activity by

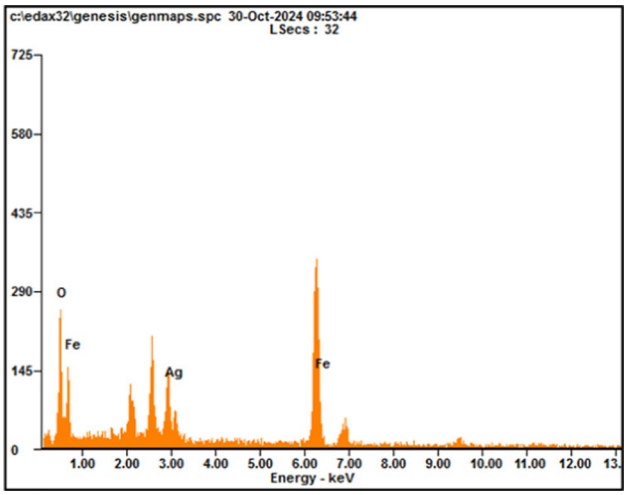

Fig. 8 EDX spectra of Ag@Fe_2O_3 nanostructure

acting as an electron regeneration center and thus reducing charge carrier recombination that leads to increased production of reactive oxygen species (ROS).

The EDX spectrum of the nanostructure, as shown in Fig. 8, shows the confirmation of only Ag (5.03%), Fe (19.93%), and O (75.04%) elements having atomic percentages (Table 1). The increase in the oxygen content and the formation of oxygen vacancies in the Fe_2O_3 lattice may explain improved photocatalytic activity [15, 32, 33].

3.5 TEM-SAED analysis

The TEM-SAED analysis was used to study the morphological characteristics and microstructural features of the synthesized Ag@Fe_2O_3 nanostructures (Figs. 9 and 10).

The images show an echinus-like morphology with an average particle size of around 35 nm, which agrees with XRD data associated with a relatively uniform particle size distribution. It was observed that lattice planes (interplanar spacing of 226 pm) correspond to the Fe_2O_3 planes (110). The SAED pattern is a series of diffraction rings indicating the polycrystalline nature. These diffraction rings can also be the plane of Fe_2O_3 crystallography, further supporting the phase purity associated with the nanoscale structures obtained [15, 16].

3.6 Line profile analysis

This analysis gives insight into the interplanar spacing and dimensions of the crystallites in the Ag@Fe_2O_3 nanostructures (Fig. 11). The intensity fluctuations noticed in the line profile are fingerprints of the lattice planes that appear in the HR-TEM images. The interplanar spacing, reduced from the peak-to-peak measurements in the line profile, is about 0.226 nm. The Scherrer equation can be used to estimate the crystallite dimensions using the FWHM of the peaks in the line profile.

A decrease in FWHM suggests an increase in the dimension of the crystallite. In this case, the relatively sharp peaks in the line profile suggest that Ag@Fe_2O_3 has a relatively large crystallite dimension, which is well supported by the observations from SEM and TEM images. The integration of line profile analysis with the data from HR-TEM and SAED provides a comprehensive understanding of the structural features of the nanostructures. Crystallite size and interplanar spacing should be precisely controlled to improve the photocatalytic activity of these materials [32, 39, 40].

Table 1 Elemental composition of Ag@Fe_2O_3 nanostructure

Element	Weight %	Atomic %
O (K)	42.03	75.04
Ag (K)	19.01	5.03
Fe (K)	38.96	19.93
Total	100%	100%

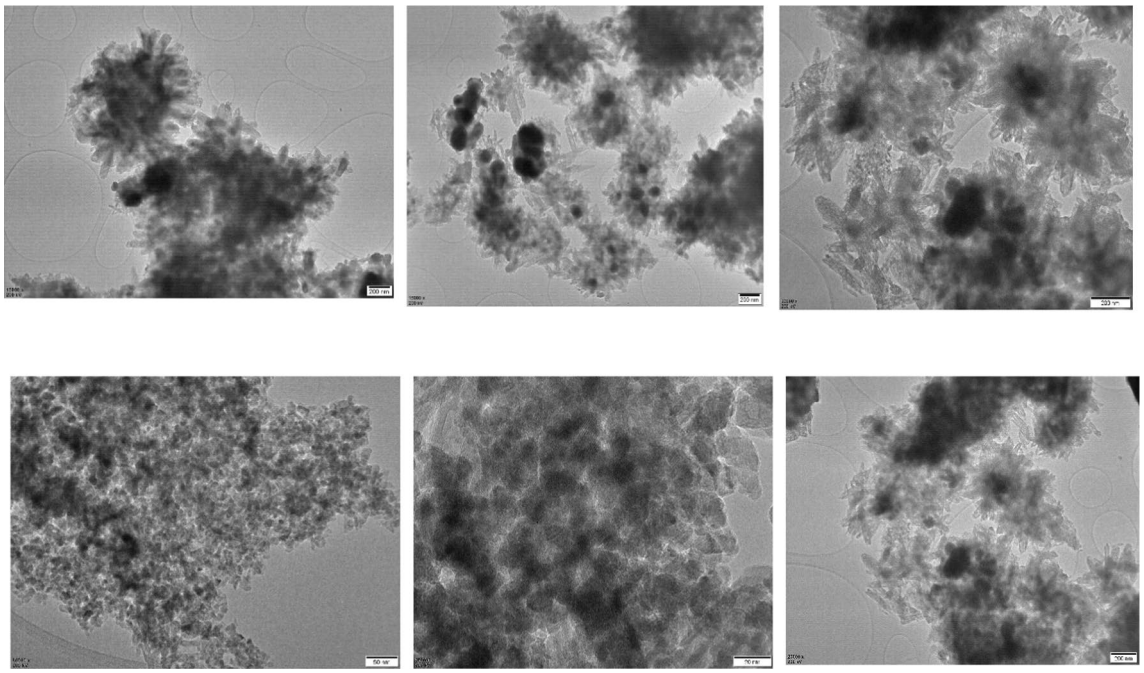

Fig. 9 TEM image of $Ag@Fe_2O_3$ nanostructure

3.7 Photocatalytic MB dye degradation mechanism by $Ag@Fe_2O_3$ nanostructure

The photoexcitation of the nanostructure in an aqueous solution during the photocatalytic dye degradation produces radicals and charged particles (Eqs. 5 to 9). Upon the absorption of photons by $Ag@Fe_2O_3$, electron–hole pairs may be generated, the mechanism of photocatalytic dye degradation as shown in the below Fig. 12;

$$Ag@Fe_2O_3 + hv\ (UV)\ Ag@Fe_2O_3 * (e_{CB-} + h_{VB+}) \tag{4}$$

Here, $Ag@Fe_2O_3$* represents the excited state, e_{CB}– and h_{VB+} Represent photoelectron (conduction band) & holes (Valence band) resp. (Eq. 4) The photogenerated holes directly oxidate the MB dye into reactive intermediates. The O_2 & H_2O involved in the indirect process are adsorbed onto the surface of the photocatalyst, producing unstable $^{\bullet}OH$ & $^{\bullet}O_2^-$, which subsequently lead to the oxidation of MB dye into their corresponding CO_2 & H_2O (Eq. 8 and 9).

$$h_{VB+} + MB - -- \rightarrow MB^+ - -- \rightarrow \ Oxidation\ of\ MB \tag{5}$$

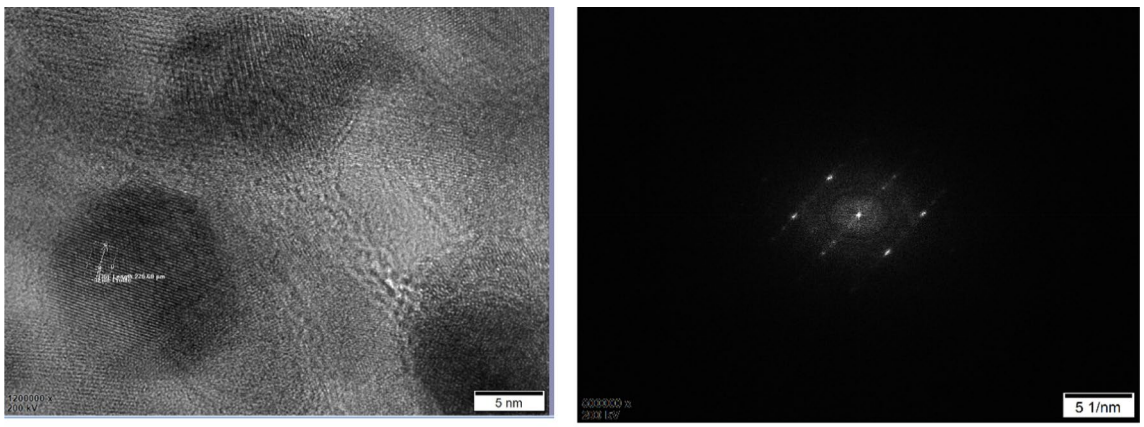

Fig. 10 **a** HR-TEM image and **b** SAED image of $Ag@Fe_2O_3$ nanostructure

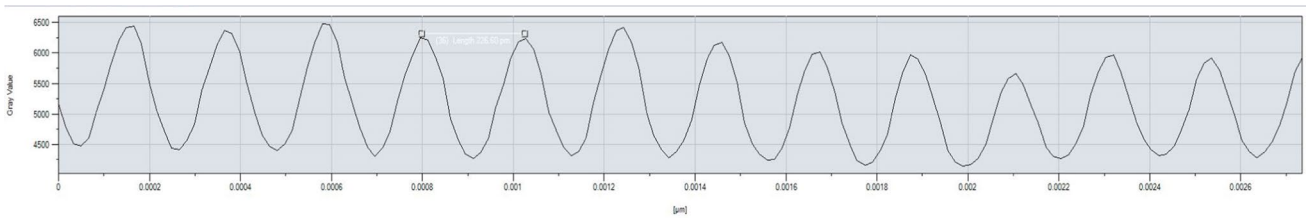

Fig. 11 Line profile of $Ag@Fe_2O_3$ nanostructure

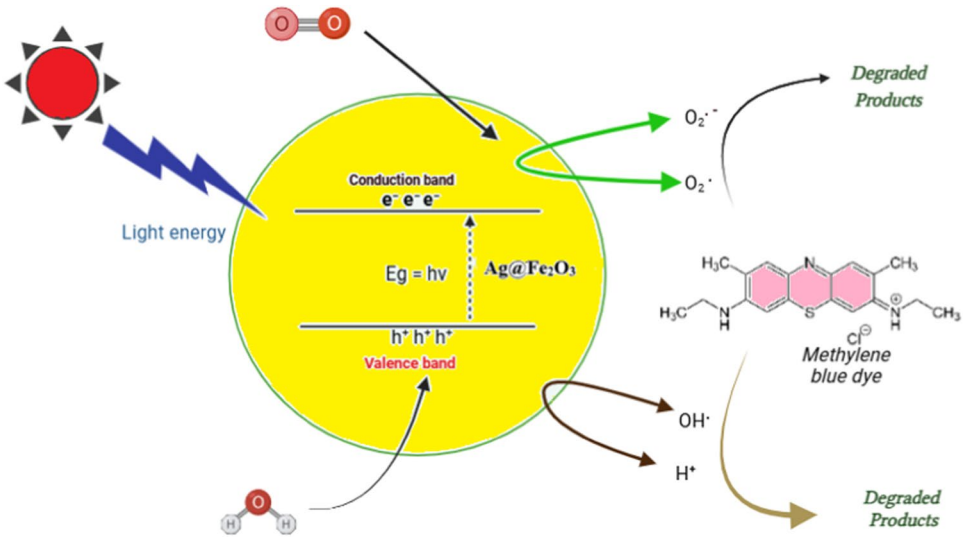

Fig. 12 Mechanism of photocatalytic MB dye degradation using $Ag@Fe_2O_3$ nanostructure

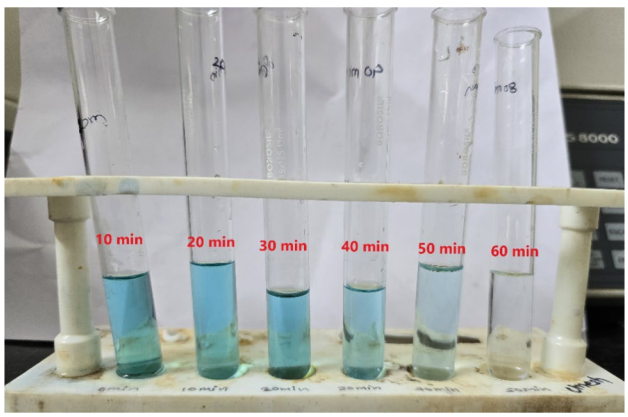

Fig. 13 MB dye solution at different time (min) interval

$$O_2 + e^-_{CB} - - - \rightarrow O_2^- \quad (6)$$

$$H_2O + h^+_{VB} - - - - \rightarrow OH^{\cdot} + H^+ \quad (7)$$

$$O_2^{-\cdot} + MB\ dye - - - - \rightarrow CO_2 + H_2O \quad (8)$$

$$OH^{\cdot} + MB\ dye - - - - \rightarrow CO_2 + H_2O \quad (9)$$

The MB dye degraded 97.10% by introducing 10 mg/L of the nanostructure.

Table 2 Absorbance and rate constant of MB dye at different time intervals

Time (min)	Absorbance [A]	Log [A]	Rate constant (K) min^{-1}	Mean (K) min^{-1}
10	0.7458	−0.1274	2.786×10^{-2}	3.025×10^{-2}
20	0.6603	−0.1803	2.002×10^{-2}	
30	0.6299	−0.2007	1.491×10^{-2}	
40	0.3954	−0.4029	2.283×10^{-2}	
50	0.1555	−0.8083	3.693×10^{-2}	
60	0.0285	−1.5451	5.90×10^{-2}	

3.7.1 Kinetic modelling of dye degradation

Using nanostructures, the photocatalytic degradation of MB dye under UV–Vis light was monitored through absorbance measurements at various time intervals (Fig. 13 and Table 2).

The consistent half-life of 22.90 min strongly indicates first-order kinetics, suggesting that the degradation rate is directly related to the dye concentration. This finding aligns with a mechanistic model where dye molecules either decompose unimolecular or react with a reactant that remains at a constant concentration.

As shown in Table 2, the absorbance decreases with time and is directly proportional to the decrease in concentration due to the dye degradation process (Fig. 14).

The percentage of degradation formula is shown in Eq. 10:

$$Dye\ degradation\ (\%) = \frac{C_0 - C}{C_0} \times 100 \tag{10}$$

[C_0 = initial concentration, C = concentration at t].

Here, C_0 (absorbance) = 0.9854, C (absorbance) = 0.0285 at t = 60 min

$$Dye\ degradation\ (\%) = \frac{0.9854 - 0.0285}{0.9854} \times 100$$

$$Dye\ degradation\ (\%) = 97.10\% \tag{11}$$

The results of the percentage of dye degradation in Table 3 indicate increased degradation over time. Its degradation efficiency rises from 24.31% at 10 min to 97.10% at 60 min (Eq. 11). Therefore, Ag@Fe_2O_3 nanostructures are promising photocatalysts compared with previously published work (Table 4).

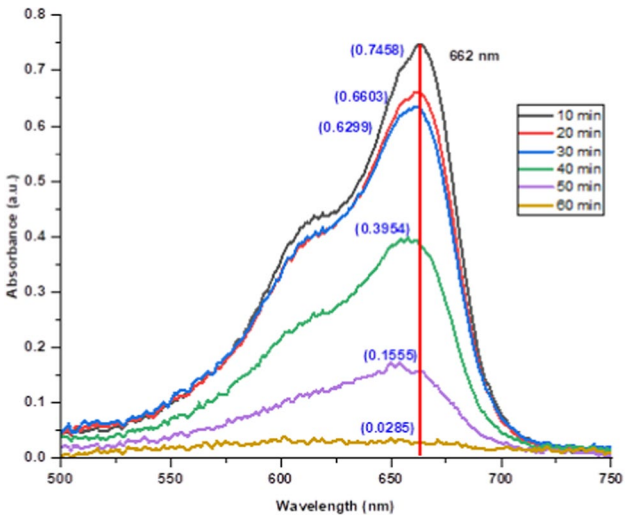

Fig. 14 Absorbance vs wavelength (nm) of MB dye degradation

Table 3 % of MB dye degradation using $Ag@Fe_2O_3$ nanostructure

Time	% dye degradation	$[A] = [A]_0 e^{-K1/t}$
10 min	24.31	0.9824
20 min	32.99	0.9839
30 min	36.07	0.9844
40 min	59.87	0.9847
50 min	84.22	0.9848
60 min	97.10	0.9849

Table 4 Comparison with previously published work of silver-doped iron oxide nanomaterials

Materials	Method	Dye degradation	Reference
$Ag@Fe_2O_3$	Hydrothermal *(Saussurea obvallata)*	97.10% (MB dye) in 60 min	This study
$Ag@Fe_2O_3$	Green synthesis (*Cabbage Peel*)	78% (phenol red) in 8 min	[13]
$Ag_3PO_4/Fe_3O_4/CS$	Co-precipitation	95% (MB)	[41]
$Ag@Fe_2O_3$	Biogenic synthesis (*Kulekhara Leaves*)	100% (crystal violet and malachite green) in 3 min	[42]
$Ag@Fe_2O_3$	Green synthesis (*Cocos nucifera L*)	High (MB dye)	[43]
$Ag/CS–Fe_2O_3$	Co-precipitation	99.44% (MB dye)	[44]
Fe_3O_4/Ag	Co-precipitation	High (Rhodamine B)	[45]
α-Fe_2O_3–Ag–ZnO	Green synthesis (*Poinciana Leaf*)	99% (Rhodamine B) in 45 min	[46]

Improving the efficiency of photodegradation may be a synergistic effect between Ag and Fe_2O_3, which inhibit the back regeneration of e^- and h^+ pairs, thus prolonging the life of the charge carriers. The generation of hydroxyl radicals ($OH^{\cdot}$) will enhance the degradation rate of the dye.

Further investigations also include assessing the rate constant, for instance, through a percentage degradation-time plot from which the slope can be determined (Fig. 15). A steep slope signifies a rapid rate. Alternatively, the reaction order can be determined using suitable plots; a concentration versus time plot's slope reflects the order of the reaction (Table 5).

The theoretical Langmuir Hinshelwood kinetic framework was used to analyze the results [47], associated with heterogeneous methods. The degradation of MB solutions in the presence of UV–Vis light incorporating $Ag@Fe_2O_3$ nanostructures shows first-order kinetics (Eq. 12 and 13).

$$\boldsymbol{R} = \frac{\boldsymbol{d}[\boldsymbol{A}]}{\boldsymbol{dt}} = \boldsymbol{K_{app}C} \tag{12}$$

where R = rate of photocatalytic degradation (mg/L.min), A = absorbance of the dye, t = duration of irradiation, and K_{app} = apparent rate constant of degradation (min^{-1}). The integrated equation gives the subsequent relationship [47].

$$\boldsymbol{K_{app}}.[\mathrm{A}] = \boldsymbol{ln}\frac{[\boldsymbol{A}]_0}{[\boldsymbol{A}]} \tag{13}$$

$[A]_0$ represents the baseline absorbance within the bulk solution at time t = 0. It has been established that the plot depicting log[*A*] Versus irradiation time (Fig. 16) adheres to a linear kinetic correlation. The half-life duration ($t_{1/2}$) was computed using the subsequent Eq. 14.

$$\boldsymbol{t}_{\frac{1}{2}} = \frac{0.693}{\boldsymbol{K}} \tag{14}$$

This result shows that the photocatalytic process effectively removes the dye from the aqueous solution.

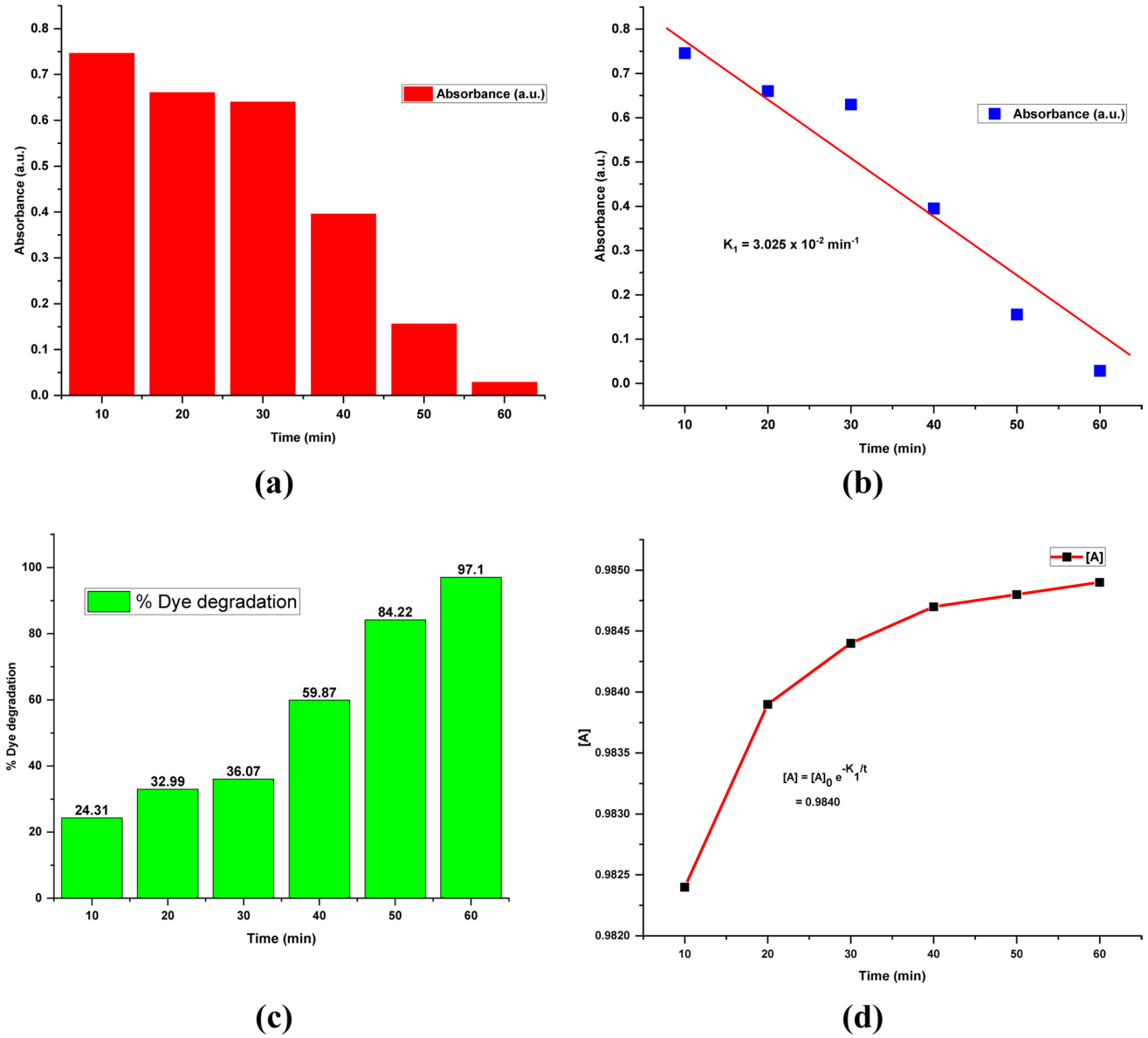

Fig. 15 **a** and **b** absorbance vs. time; **c** % of MB dye degradation vs. time (min); **d** [A] vs. time

Table 5 Pearson correlation coefficient; (absorbance (X) of dye vs. time (Y)

X—Mx	Y—My	$(X—Mx)^2$	$(Y—My)^2$	(X—Mx)(Y—My)
−25	0.31	625	0.096	−7.748
−15	0.224	225	0.05	−3.366
−5	0.194	25	0.038	−0.97
5	−0.041	25	0.002	−0.203
15	−0.28	225	0.079	−4.206
25	−0.407	625	0.166	−10.185
Mx: 35.000	My: 0.436	Sum: 1750.000	Sum: 0.430	Sum: −26.677

Where, Mx = Mean of all x values; My = Mean of all Y values; $\Sigma(X—Mx)^2$ = Sum of Squares of X (SSx); $\Sigma(Y—My)^2$ = Sum of Squares of Y (SSy); $\Sigma(X—Mx)(Y—My)$ = Sum of products (Fig. 5). The calculated correlation coefficient is r = −0.9722, indicating a strong negative correlation between the chosen X and Y variables. In the context of photocatalytic dye degradation, a strong inverse relationship between factors like irradiation time and the natural logarithm of the normalized dye concentration would be expected for a pseudo-first-order reaction. The value of R^2, the coefficient of determination, is 0.9452

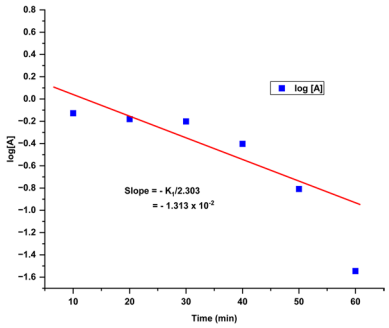

Fig. 16 Langmuir Hinshelwood plot for MB dye degradation using Ag@Fe_2O_3 nanostructure

4 Conclusion

The Ag@Fe_2O_3 nanostructures are produced through an eco-friendly method using an aqueous extract of Saussurea obvallata leaves, which serve as reducing and capping agents. TEM images reveal that the resulting nanostructures exhibit an echinus-like morphology, with an estimated particle diameter of approximately 35 nm. EDX analysis verified the presence of the elements Ag, Fe, and O within the nanostructures. The crystalline properties of the nanostructures were analyzed using TEM and SAED measurements. It was found that the interplanar spacing measures approximately 0.226 nm, corresponding to the distance between the (110) planes of Fe_2O_3. The nanostructures' photocatalytic activity was evaluated by monitoring the degradation of MB dye under UV–Vis light irradiation. This nanostructure exhibits remarkable photocatalytic performance; 60 min was sufficient for substantial degradation of the MB dye. The enhanced photocatalytic activity may stem from the synergistic interplay between Ag and Fe_2O_3 nanoparticles, the unique echinus-like morphology, and impressive charge separation and transfer capabilities. These nanostructures are highly promising for boosting the photo-photocatalytic efficiency in degrading organic waste generated by wastewater treatment technologies. Ongoing research into the practical use of these nanostructures for water treatment, environmental remediation, and energy storage reveals exciting future possibilities.

Author contributions Vikram Jadhav: Writing—Original Draft, investigation, methodology. Yash Dhanwate: Supervision, Resources, Validation, Pradnya Raut: Conceptualization, Data Curation. Shilpa Shinde: Editing, Investigation, Formal Analysis, Rajashri Sawant: Writing—Original Draft, Resources, Arun Bhagare: Writing—Review & Editing.

Data availability Data is provided within the manuscript or supplementary information files.

Declarations

Ethical approval and consent to participate The plant materials utilized in this study were collected in compliance with local/national guidelines, and no further permissions were required.

Competing interests The authors declare no competing interests.

References

1. Vasudeo Rane A, Thomas S, Kalarikkal N. Microscopy applied to materials sciences and life sciences. Apple Academic Press; 2018.
2. Kavil YN, et al. The removal of methylene blue as a remedy of dye-based marine pollution: a photocatalytic perspective. Res Chem Intermed. 2020;46(1):755–68. https://doi.org/10.1007/s11164-019-03988-w.

3. Agarwal S, et al. Efficient removal of toxic bromothymol blue and methylene blue from wastewater by polyvinyl alcohol. J Mol Liq. 2016;218:191–7. https://doi.org/10.1016/j.molliq.2016.02.060.
4. Khan I, et al. Review on Methylene Blue: Its Properties, Uses, Toxicity and Photodegradation. Water (Basel). 2022;14(2):242. https://doi.org/10.3390/w14020242.
5. Begum R, et al. Chemical reduction of methylene blue in the presence of nanocatalysts: a critical review. Rev Chem Eng. 2020;36(6):749–70. https://doi.org/10.1515/revce-2018-0047.
6. Cwalinski T, et al. Methylene blue—current knowledge, fluorescent properties, and its future use. J Clin Med. 2020;9(11):3538. https://doi.org/10.3390/jcm9113538.
7. Wu C-H, Chern J-M. Kinetics of photocatalytic decomposition of methylene blue. Ind Eng Chem Res. 2006;45(19):6450–7. https://doi.org/10.1021/ie0602759.
8. Din MI, Khalid R, Najeeb J, Hussain Z. Fundamentals and photocatalysis of methylene blue dye using various nanocatalytic assemblies- a critical review. J Clean Prod. 2021;298: 126567. https://doi.org/10.1016/j.jclepro.2021.126567.
9. Yang Y-Y, He M-Q, Li M-X, Huang Y-Q, Chi T, Wang Z-X. Ferrimagnetic copper-carboxyphosphinate compounds for catalytic degradation of methylene blue. Inorg Chem Commun. 2018;94:5–9. https://doi.org/10.1016/j.inoche.2018.05.026.
10. Baste Y, et al. Polyol synthesis of ag-doped copper oxide nanoparticles as a methylene blue-degrading agent. Catalysts. 2023;13(7):1143. https://doi.org/10.3390/catal13071143.
11. Yang C, et al. High selectivity of Ag-doped Fe_2O_3 hollow nanofibers in H2S detection at room operating temperature. Sens Actuators B Chem. 2021;341: 129919. https://doi.org/10.1016/j.snb.2021.129919.
12. Verma R, et al. Silver ions modified α-Fe_2O_3 nanoparticles: an efficient antibacterial agent for multidrug resistant bacteria. J Clust Sci. 2024;35(7):2511–23. https://doi.org/10.1007/s10876-024-02680-3.
13. Idris DS, Roy A. Antioxidant and dye degradation activity of green synthesized silver-iron oxide (Ag-Fe_2O_3) bimetallic nanoparticles. Nano-Struct Nano-Objects. 2024;38: 101142. https://doi.org/10.1016/j.nanoso.2024.101142.
14. Biabani-Ravandi A, Rezaei M, Fattah Z. Catalytic performance of Ag/Fe_2O_3 for the low temperature oxidation of carbon monoxide. Chem Eng J. 2013;219:124–30. https://doi.org/10.1016/j.cej.2012.12.094.
15. Das BR, Jena S, Dhal JP. Ag doped α-Fe_2O_3 nanoparticles: synthesis, characterization and application as heterogeneous photocatalyst for removal of organic dye from aqueous media without any oxidizing agents. J Indian Chem Soc. 2021;98(11): 100214. https://doi.org/10.1016/j.jics.2021.100214.
16. Kumar S, Kumar A, Malhotra T, Verma S. Characterization of structural, optical and photocatalytic properties of silver modified hematite (α-FeO) nanocatalyst. J Alloys Compd. 2022;904: 164006. https://doi.org/10.1016/j.jallcom.2022.164006.
17. Watanabe A, Kozuka H. Photoanodic properties of sol−gel-derived Fe_2O_3 thin films containing dispersed gold and silver particles. J Phys Chem B. 2003;107(46):12713–20. https://doi.org/10.1021/jp0303568.
18. Jadhav VR, Aher JS, Bhagare AM, Dhaygude AC, Lokhande DD. Plant-mediated green synthesis of nanoparticles for photocatalytic dye degradation. In: Shah MP, Roy A, editors. Phytonanotechnology. Singapore: Springer Nature Singapore; 2022. p. 31–57. https://doi.org/10.1007/978-981-19-4811-4_2.
19. Vijayaraghavan K, Ashokkumar T. Plant-mediated biosynthesis of metallic nanoparticles: a review of literature, factors affecting synthesis, characterization techniques and applications. J Environ Chem Eng. 2017;5(5):4866–83. https://doi.org/10.1016/j.jece.2017.09.026.
20. Thomas S, Rouxel D, Jose S. Green composites: material for a sustainable world. Emerg Mater. 2022;5(3):601–2. https://doi.org/10.1007/s42247-022-00395-7.
21. Shanker U, Vipin, Rani M, Metal oxides–based nanomaterials: green synthesis methodologies and sustainable environmental applications. Handbook of Green and Sustainable Nanotechnology. Cham: Springer International Publishing; 2023. p. 1–27. https://doi.org/10.1007/978-3-030-69023-6_80-2.
22. Shams S, et al. Facile and eco-benign synthesis of Au@Fe_2O_3 nanocomposite: Efficient photocatalytic, antibacterial and antioxidant agent. J Photochem Photobiol B. 2019;199: 111632. https://doi.org/10.1016/j.jphotobiol.2019.111632.
23. Kumar P, Pathak D, Thakur N. Trimetallic doped hematite (α-Fe_2O_3) nanoparticles using biomolecules of Azadirachta indica leaf extract for photocatalytic dye removal: insights into catalyst stability and reusability. Emerg Mater. 2024. https://doi.org/10.1007/s42247-024-00742-w.
24. Zouari Ahmed R, et al. Green synthesis of α-Fe_2O_3 and α-Fe_2O_3@Ag NC for degradation of rose Bengal and antimicrobial activity. Biomass Convers Biorefin. 2023;15(1):255–69. https://doi.org/10.1007/s13399-023-05046-3.
25. Mukhopadhyay N, Jain D, Tripathi A, Bhaskar P. A comprehensive insight into the pharmaceutical potential of saussurea obvallata. Curr Pharmacol Rep. 2024;10(6):349–59. https://doi.org/10.1007/s40495-024-00370-2.
26. Semwal P, Painuli S. Antioxidant, antimicrobial, and GC-MS profiling of Saussurea obvallata (Brahma Kamal) from Uttarakhand Himalaya. Clinical Phytosci. 2019;5(1):12. https://doi.org/10.1186/s40816-019-0105-3.
27. Kumar J, Pundir M. Phytochemistry and pharmacology of Saussurea genus (Saussurea lappa, Saussurea costus, Saussurea obvallata, Saussurea involucrata). Mater Today Proc. 2022;56:1173–81. https://doi.org/10.1016/j.matpr.2021.11.145.
28. Vidya Sagar PSR, Ramadevi D, Basavaiah K, Botsa SM. Green synthesis of silver nanoparticles using aqueous leaf extract of Saussurea obvallata for efficient catalytic reduction of nitrophenol, antioxidant, and antibacterial activity. Water Sci Eng. 2024;17(3):274–82. https://doi.org/10.1016/j.wse.2023.09.004.
29. Gao N, Chen Y, Jiang J. Ag@Fe_2O_3-GO nanocomposites prepared by a phase transfer method with long-term antibacterial property. ACS Appl Mater Interfaces. 2013;5(21):11307–14. https://doi.org/10.1021/am403538j.
30. Kaur G, Divya, Khan SA, Satsangi VR, Dass S, Shrivastav R. Nano-hetero-structured thin films, ZnO/Ag-(α)Fe_2O_3, with n/n junction, as efficient photoanode for renewable hydrogen generation via photoelectrochemical water splitting. Renew Energy. 2021;164:156–70. https://doi.org/10.1016/j.renene.2020.09.060.
31. Reddy IN, Reddy ChV, Sreedhar A, Cho M, Kim D, Shim J. Effect of plasmonic Ag nanowires on the photocatalytic activity of Cu doped Fe_2O_3 nanostructures photoanodes for superior photoelectrochemical water splitting applications. J Electroanal Chem. 2019;842:146–60. https://doi.org/10.1016/j.jelechem.2019.04.076.

32. Jasrotia T, Chaudhary S, Kaushik A, Kumar R, Chaudhary GR. Green chemistry-assisted synthesis of biocompatible Ag, Cu, and Fe_2O_3 nanoparticles. Mater Today Chem. 2020;15: 100214. https://doi.org/10.1016/j.mtchem.2019.100214.
33. Al-Zahrani FAM, Al-Zahrani NA, Al-Ghamdi SN, Lin L, Salem SS, El-Shishtawy RM. Synthesis of Ag/Fe_2O_3 nanocomposite from essential oil of ginger via green method and its bactericidal activity. Biomass Convers Biorefin. 2024;14(12):13265–73. https://doi.org/10.1007/s13399-022-03248-9.
34. Park K, Hong HY, Jung GW, Kim DH, Hakeem DA, Iqbal A. Structural and thermoelectric properties of hydrothermal-processed Ag-doped Fe_2O_3. Ceram Int. 2018;44(13):15024–34. https://doi.org/10.1016/j.ceramint.2018.05.132.
35. Gu Y, et al. Magnetic hyperthermia with ε-Fe_2O_3 nanoparticles. RSC Adv. 2020;10(48):28786–97. https://doi.org/10.1039/D0RA04361C.
36. Karthik L, Kumar G, Kirthi AV, Rahuman AA, Bhaskara Rao KV. Streptomyces sp. LK3 mediated synthesis of silver nanoparticles and its biomedical application. Bioprocess Biosyst Eng. 2014;37(2):261–7. https://doi.org/10.1007/s00449-013-0994-3.
37. Mandal S, Samanta PK. Rietveld analysis of X-ray diffraction pattern of sol-gel synthesized copper oxide nanoparticles. Mater Today Proc. 2022;60:1051–5. https://doi.org/10.1016/j.matpr.2022.01.242.
38. Roba S, Negera D, Abebe B. Ag-Fe_2O_3 nanocomposites for synergistically enhanced antibacterial activity. Inorg Chem Commun. 2024;160:112019. https://doi.org/10.1016/j.inoche.2024.112019.
39. Reddy ChV, Reddy IN, Sreedhar A, Shim J. Investigation of dopant and Ag plasmonic effect on α-Fe_2O_3 photoelectrode for photoelectrochemical water splitting activity. Appl Surf Sci. 2019;488:629–38. https://doi.org/10.1016/j.apsusc.2019.05.316.
40. Jang JS, Yoon KY, Xiao X, Fan F-RF, Bard AJ. Development of a Potential Fe_2O_3-based photocatalyst thin film for water oxidation by scanning electrochemical microscopy: effects of Ag–Fe_2O_3 nanocomposite and Sn doping. Chem Mater. 2009;21(20):4803–10. https://doi.org/10.1021/cm901056c.
41. Somasundaram AJ, Elanthamilan E, Wang S-F, Lydia IS. Construction of magnetic Ag3PO4/Fe3O4/Chitosan polymer composite with enhanced visible-light-driven photocatalytic activity for the Methylene blue dye degradation. J Polym Environ. 2024;32(12):6650–66. https://doi.org/10.21203/rs.3.rs-4568116/v1.
42. Kolya H, Kang C-W. Biogenic synthesis of silver-iron oxide nanoparticles using kulekhara leaves extract for removing crystal violet and malachite green dyes from water. Sustainability. 2022;14(23):15800. https://doi.org/10.3390/su142315800.
43. Mohan NS, Rifaya MA, Manivannan J, Vijayalakshmi V, Synthesis and characterization of Fe_2O_3, Fe_2O_3@Ag, Fe_2O_3 @AC and Fe_2O_3 @Ag@AC NCs for waste water treatment applications. Novel Aspects on Chemistry and Biochemistry. B P International (a part of SCIENCEDOMAIN International); 2023, vol. 7, p. 40–50. https://doi.org/10.9734/bpi/nacb/v7/6739A.
44. Zain Ul Abidin M, et al. Catalytic degradation of methylene blue and bactericidal action by silver and CS-doped iron oxide nanostructures: experimental and DFT approaches. Mater Chem Phys. 2023;308:128300. https://doi.org/10.1016/j.matchemphys.2023.128300.
45. Nchimi Nono K, Vahl A, Terraschke H. Towards high-performance photo-fenton degradation of organic pollutants with magnetite-silver composites: synthesis, catalytic reactions and in situ insights. Nanomaterials. 2024;14(10):849. https://doi.org/10.3390/nano14100849.
46. Salem KH, et al. Eco-friendly synthesis of γ-Fe_2O_3–Ag–ZnO nanocomposite with antibacterial and RhB dye degradation properties using leaf extract. Int J Nanosci. 2024;23(04):2350088. https://doi.org/10.1142/S0219581X23500886.
47. Kalaycıoğlu Z, Özuğur Uysal B, Pekcan Ö, Erim FB. Efficient photocatalytic degradation of methylene blue dye from aqueous solution with cerium oxide nanoparticles and graphene oxide-doped polyacrylamide. ACS Omega. 2023;8(14):13004–15. https://doi.org/10.1021/acsomega.3c00198.